Eur. Phys. J. E (2017) **40**: 28
DOI 10.1140/epje/i2017-11516-6

THE EUROPEAN PHYSICAL JOURNAL E

Regular Article

Action of fields on captive disclination loops

Mallory Dazza[1,2], Rui Cabeça[3], Simon Čopar[4], Maria Helena Godinho[3], and Pawel Pieranski[1,a]

[1] Laboratoire de Physique des Solides, Université Paris-Sud, Bât. 510, 91405 Orsay, France
[2] École normale supérieure de Cachan, 61 Avenue du Président Wilson, 94235 Cachan, France
[3] CENIMAT, Faculdade de Ciências e Tecnologia - Universidade Nova de Lisboa, 2829 - 516 Caparica, Portugal
[4] Faculty of Mathematics and Physics, University of Ljubljana, Jadranska 19, 1000 Ljubljana, Slovenia

Received 7 December 2016
Published online: 20 March 2017 –

Abstract. We report on two effects observed in experiments with captive disclination loops on polymeric fibers immersed in nematics and submitted to electric and/or magnetic fields. We show that the magnetic field oblique to a fiber with axial or helicoidal anchoring on its surface induces translation of disclination loops. Fields orthogonal to fibers with helicoidal anchoring make disclination loops rotate around the field direction. In the linear regime of this last chirogyral effect, the angle of rotation is proportional to the helix wave vector and its sense unveils the chirality of the helix. We propose a model explaining the origin and all features of these two effects.

1 Introduction

1.1 Free disclination loops in bulk nematics

Disclination lines are linear topological defects characteristic of the director field **n** in nematic liquid crystals. Let us remind that the name "nematic" coined by George Friedel [1] stems from the Greek word $\nu\eta\mu\alpha$ (thread) and refers to these defects, which, when observed in a microscope, appear as thin threads. Because of their topological nature disclinations never terminate in bulk but are always either spanned between solid surfaces or form closed loops.

Due to their tension T (energy per unit length), disclination loops immersed in bulk nematics have the tendency to shrink and finally to collapse. As an example we show in fig. 1 a thick layer (large flat droplet) of the nematic 5CB spread on a glass slide treated for homeotropic anchoring. Disclination loops 1, 2 and 3 have been generated by a gentle stirring of the nematic with a pipette tip. The series of four pictures shows that all three disclination loops shrink and end (or will end) to collapse. Let us emphasize that the collapse of these loops is traceless which means that their topological charge is null.

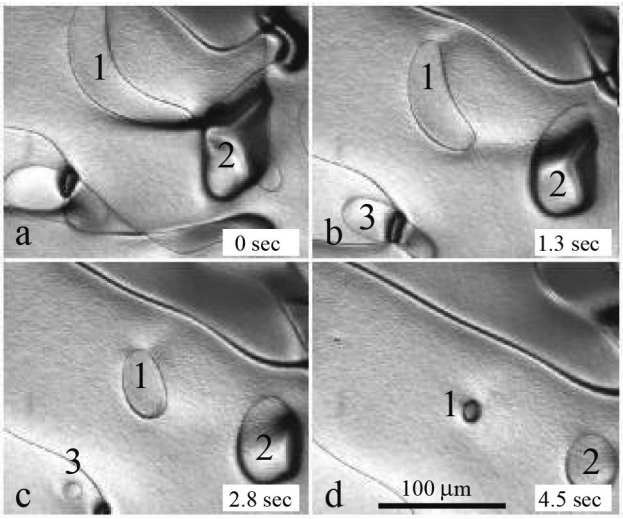

Fig. 1. Shrinking disclination loops in a thick layer of the nematic 5CB spread on a glass plate with homeotropic boundary conditions. The upper surface of the nematic layer is free. Disclination loops 1, 2 and 3 generated by a gentle stirring of the droplet with a pipette tip are shrinking from a to d and finally collapse. View in a microscope in non-polarized light.

1.2 Free disclination loops in thin homeotropic samples

This natural tendency of disclination loops to shrink in bulk nematics can be hindered or even inverted by elastic interactions with surfaces.

Let us consider first the second case of disclination loops growing in spite of their tension. This phenomenon, illustrated in fig. 2, is well known to experimentalist preparing thin homeotropic samples such as the one in fig. 3a. The cell containing the nematic is made of two glass plates, the surfaces of which are treated for the homeotropic anchoring and which are separated and glued

[a] e-mail: pawel.pieranski@u-psud.fr

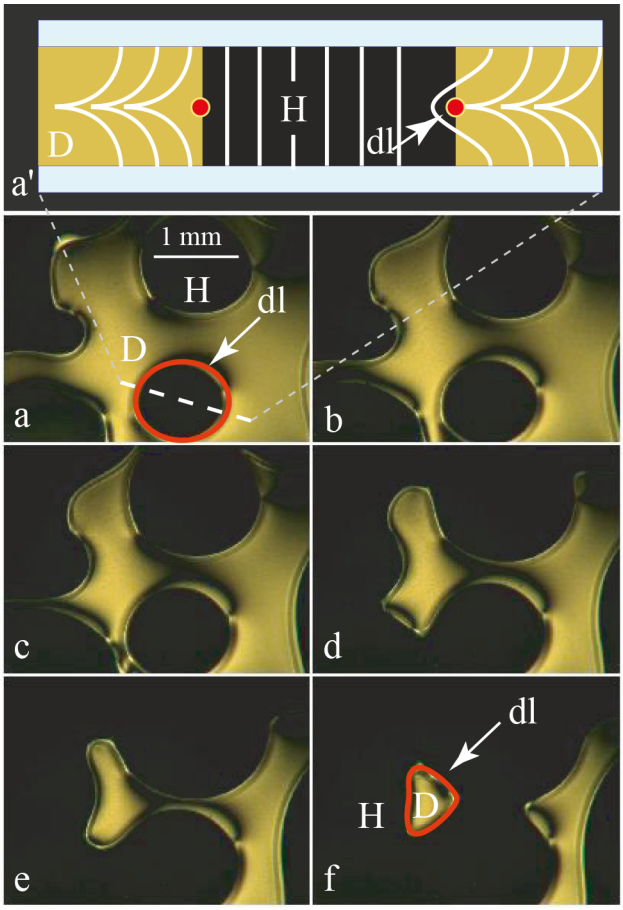

Fig. 2. Disclination loops observed during preparation of a homeotropic sample of 5CB. a,a′) a homeotropic (H) domain surrounded by the dowser (D) texture is surrounded by a disclination loop (dl) drawn with red line; b–f) growth of H-in-D domains driven by the gain in the surface elastic energy; f) a dowser-in-homeotropic domain before its collapse. Pictures a–f were taken at intervals of 15 s.

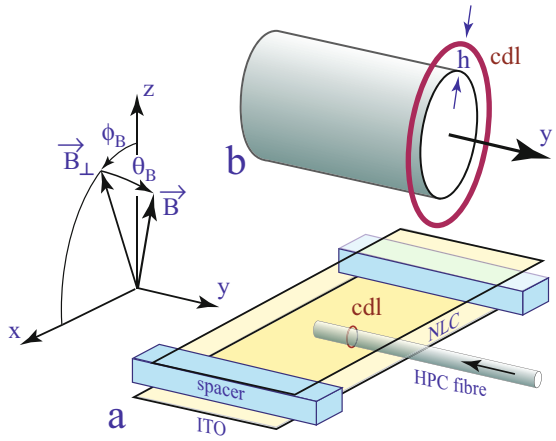

Fig. 3. The principle of first experiments with captive disclinations threaded on a HPC fiber inserted in a homeotropic sample of the nematic liquid crystal EN18: a) General view of the sample. Nematic liquid crystal (NLC) is hold by capillarity between two glass slides separated by spacers and equipped with ITO electrodes treated for homeotropic anchoring. Observation are made from the z direction by means of a video microscope. The magnetic field B is orientable as shown. b) Detailed view of a captive disclination levitating at height h above the fiber surface.

together by spacers of typical thickness $d < 100\,\mu$m. Due to the Poiseuille flow during filling of this cell with the nematic, the initial texture is not uniformly homeotropic as expected but contains initially small homeotropic domains, such as H in fig. 2a, surrounded by the texture labeled D in fig. 2a [2–5].

The label D stands for "dowser" because, as shown in fig. 2a′, in this texture the director rotates by π between the two limit plates and the director fields lines have the shape of a Y-shaped dowser rod. Moreover, this texture called also quasi-planar [2–4] or "planar" [5] has been shown recently to be very sensitive to perturbations such as magnetic fields or thickness gradients [6].

For topological reasons, the homeotropic and dowser textures in fig. 2a′ must be separated by disclinations. Therefore, all homeotropic-in-dowser (H-in-D) domains in fig. 2a must be surrounded by disclination loops. One of these loops is represented as the red line in fig. 2a.

In spite of their tension, disclination loops surrounding the H-in-D domains are growing when they are large enough. One arrives at this conclusion by comparing the gain in the elastic energy integrated on the surface of a H-in-D domain of radius R, $\Delta F_{\rm el} \approx -(\pi^2 K/d)\pi R \Delta R$, with the cost of elongation of the disclination $\Delta F_{\rm dis} = T 2\pi \Delta R$. The total change in energy $\Delta F_{\rm el} + \Delta F_{\rm dis}$ is negative when the radius R is larger than

$$R_c = \frac{2}{\pi^2}\frac{T}{K}d. \qquad (1)$$

A more detailed calculation made in ref. [6] leads to the conclusion that $R_c \approx 2d$. The thickness of the sample in fig. 2 being $d = 0.1$ mm, the critical radius $R_c = 0.2$ mm is smaller than the radius $R = 0.5$ mm of the homeotropic domain H, so that it grows as shown in figs. 2a–f. The growth of H-in-D domains leads to their coalescence and finally to the formation of dowser-in-homeotropic (D-in-H) domains (see the domain pointed by an arrow in fig. 2f) which obviously must be surrounded by disclination loops too. Due to the sign change in the surface elastic energy $\Delta F_{\rm el} = \pi^2 (K/d) R \Delta R$, such a D-in-H disclination loop should collapse unless it is threaded on a fiber with a planar axial anchoring inserted in the homeotropic sample as shown in fig. 3a.

Let us remind that the collapse of disclination loops in nematics is known since long time to be hindered by three-dimensional inclusions. The so-called Saturn ring surrounding a spherical inclusion with homeotropic boundary conditions [7–9] is the first known realization of a captive disclination loop. Captive disclination loops of more complex shapes and topologies are also known to occur in so-called rafts of colloidal particles [10]. Here we focus on disclination loops threaded on fibers.

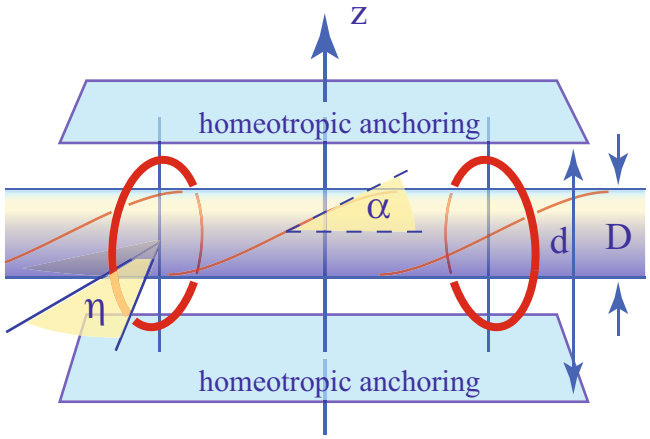

Fig. 4. The principle of the chirogyral effect. A fiber, with a planar helicoidal anchoring characterized by the angle α, is inserted in a homeotropic nematic sample. Disclination loops captive on the fiber are tilted around the z axis and make the angle η with the xy plane orthogonal to the fiber.

1.3 Captive disclination loops, the chirogyral effect

First observations of disclination loops captive on fibers were made in experiments with nematic [11] and cholesteric droplets [12] threaded on HPC fibers with planar anchoring. When the anchoring at the nematic (cholesteric)/air is homeotropic, each droplet must contain, for topological reasons, a defect with topological charge $N = 1$: a disclination loop equivalent to a radial hedgehog.

Captive disclination loops were also observed on glass fibers with homeotropic anchoring immersed in planar nematic samples [13,14]. In this geometry, disclination loops were generated in a controlled manner by the Kibble-Zurek mechanism during quenching from the isotropic into the nematic phase.

Recently, captive disclination loops were created and studied using HPC and nylon fibers with a planar anchoring immersed in homeotropic nematic samples [15]. In the case when the planar anchoring on the fiber surface was helicoidal, due to the chirality of the polymer (HPC) or to the mechanical torsion of the fiber, the so-called chirogyral effect was observed (see fig. 4): the captive disclination loops are tilted with respect to the fiber axis by the angle η which is proportional in the first approximation to the helix angle α

$$\eta = C_g(D/d)\alpha. \tag{2}$$

The chirogyral coefficient $C_g(D/d)$ occurring in this formula is a function of the ratio D/d between the fiber diameter D and the sample thickness d. In these first experiments, for symmetry reasons, disclination loops were rotating around the axis z parallel to the homeotropic anchoring on the sample surfaces.

Let us stress that the chirogyral effect was discovered previously in experiments with nematic droplets threaded on helicoidally shaped fibers obtained by electrospinning where disclination loops were tilted with respect to the average axis of fibers [16].

1.4 Aim of the present work

The aim of the present work is to study the behavior of captive disclination loops in electric and magnetic fields. In particular, we will show that in nematics with positive dielectric and magnetic anisotropies the chirogyral effect is enhanced by the application of fields. This allows to detect the chirality of fibers even when it is small.

We will show that in strong enough fields, when the magnetic coherence length ξ is much shorter than the sample thickness, the elastic interaction of loops with limit plates becomes negligible. As a result, the rotation of the disclination loops driven by the chirogyral effect occurs around the direction $\mathbf{B}_\perp$ given by the magnetic field $\mathbf{B}$ the orientation of which can be changed arbitrarily (see fig. 3). Moreover, in the limit $\xi \ll D$ the analytical model of the chirogyral effect becomes very simple.

2 Preliminary experiments

2.1 Generation of captive disclination loops by electrohydrodynamic turbulence

In the experiment illustrated by the series of eight pictures in fig. 5, a fiber of diameter $D = 28\,\mu$m, drawn by hand from an anisotropic 63% HPC-in-water solution, has been inserted in a homeotropic sample of thickness $d = 100\,\mu$m through one of its two free edges (see fig. 3a). Initially (fig. 5a) this sample contained one disclination loop threaded on the fiber. A 100 Hz, 50 V, AC voltage applied subsequently to this EN18 sample with negative dielectric anisotropy drove the electrohydrodynamic turbulence which stretched progressively the initial disclination loop and created the strongly light scattering area labelled DSM2, the size of which is growing with time [17] as shown in figs. 5b and c. After switching the excitation off, due to the elastic relaxation, the density of disclination (length/unit volume) is rapidly falling down and a tangle of individual disclinations can be distinguished in fig. 5d. In figs. 5f only three loops are left. Their evolution in figs. 5g and h shows that the one labeled "cdl" is captive and while the other two, "fdl1" and "fdl2", are free and can collapse.

The outcome of this first experiment is that the topology is a robust feature of the director field. Nevertheless, when a vigorous hydrodynamic turbulence is applied for a longer period, new captive disclinations can be created. This is shown in the series of seven pictures in fig. 6 where the number of captive disclinations increases from 1 (fig. 6b) to 13 (fig. 6h) by the generation of six pairs of captive disclinations. The mechanism of generation of a new pair of captive disclinations from one, unraveled by observations at high magnifications, is represented schematically in fig. 7. It can be decomposed in four stages:

1) Stretching of the captive disclination by the electrohydrodynamic turbulence (see fig. 7a,b).
2) Tearing out a free disclination loop from the stretched captive disclination (see fig. 7b,c).

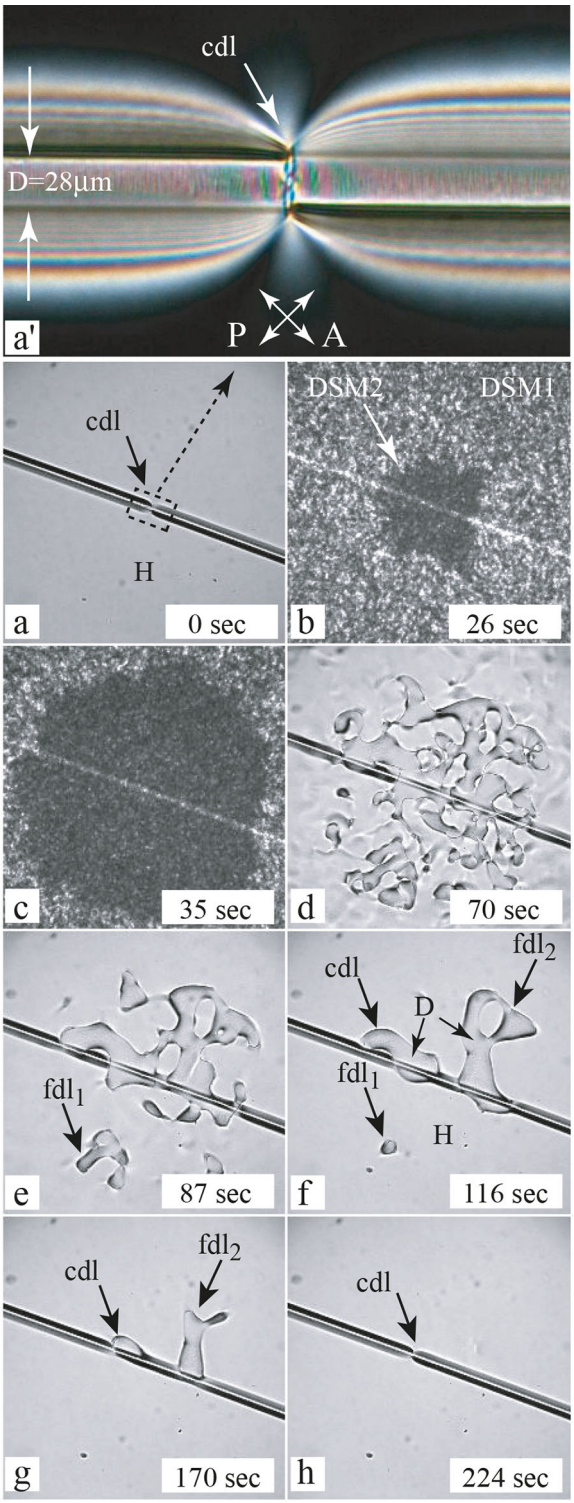

Fig. 5. Free and captive disclination loops in a homoetropic sample of the nematic EN18. a,a′) one captive disclination loop (cdl); b,c) stretching of the initial disclination loop by electrohydrodynamic turbulence; d–h) relaxation of disclination loops created by turbulence; all loops but one collapse.

3) Stretching of the free disclination loop and its and winding around the fiber (see fig. 7c,d).
4) Splitting of the stretched free disclination into a pair of two captive ones (see fig. 7d–f).

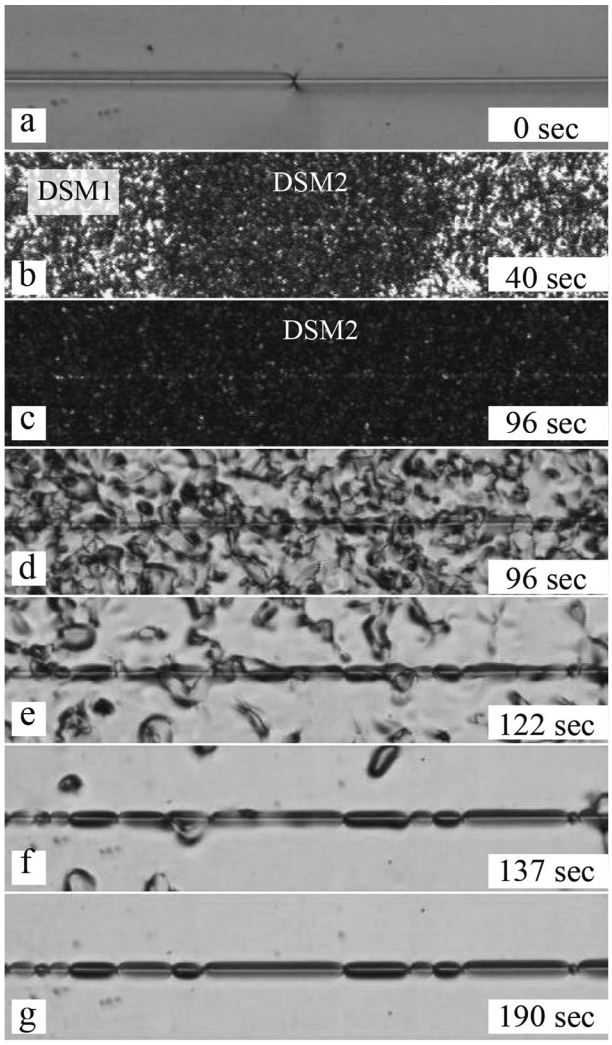

Fig. 6. Generation of captive disclination loops by the electrohydrodynamic turbulence: a) one disclination loop captive on a HPC fiber inserted in a homeotropic cell of the nematic EN18; b) stretching of the initial captive disclination loop leads to formation of the strongly light scattering domain DSM2 containing a finite density of disclinations; c) growth of the DSM2 domain; d–g) elastic relaxation after switching the AC field off unveils the existence of six new pairs of disclination loops generated by the turbulent flow.

2.2 Generation of a solitary captive disclination loop

In the method described above, the number and positions of captive disclination loops are random. The second setup (see fig. 8), tailored for the study of the chirogyral effect, allows to work with a solitary disclination loop, the position of which in the nematic sample is well controlled.

In this second setup the two glass plates are fixed on independent supports in a manner that the thickness d of the sample can be controlled (without spacers) with accuracy of $10\,\mu$m. The nematic liquid crystal is hold by capillarity between the overlapping parts of the glass plates. The sample —NLC + glass plates— is fixed on another

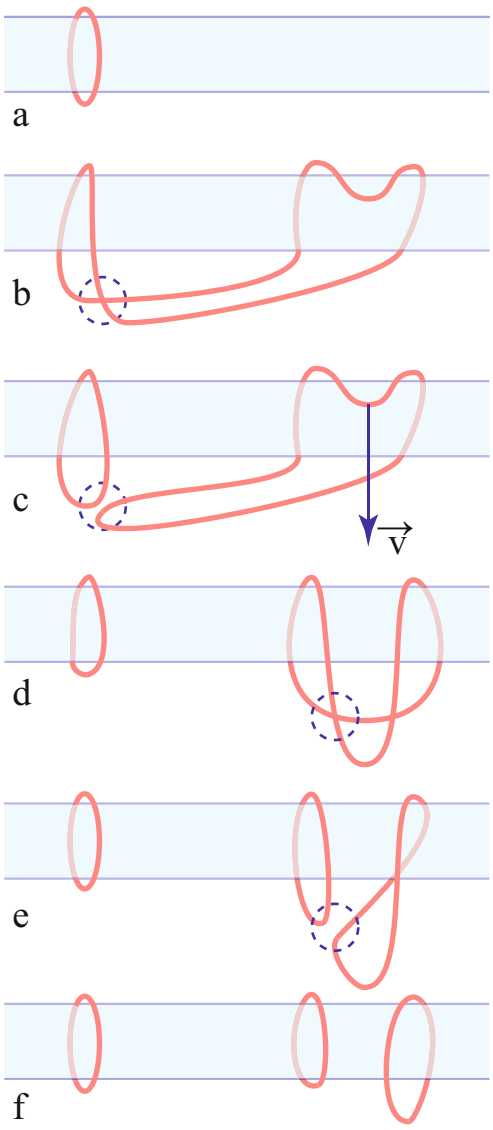

Fig. 7. Generation a new pair of disclination loops by the turbulent flow: a-b) stretching of a captive disclination loop and its winding around the fiber; b,c) collision of two section of the stretched captive disclination loop and recombination into one captive and one free disclinations; d) stretching of the free disclination loop and its winding around the fiber; d–f) collision of two section of the stretched free disclination loop and recombination into a pair of two captive disclinations.

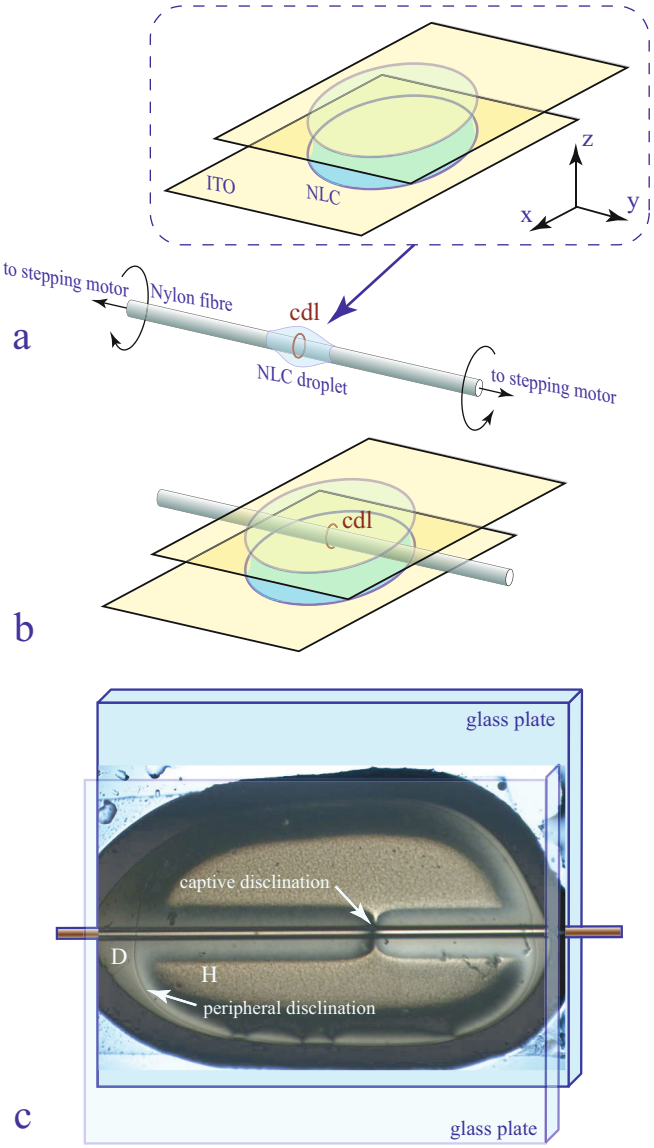

Fig. 8. The principle of the experimental setup tailored for experiments with captive disclinations threaded on a nylon fiber: a) the captive disclination loop is first contained in a small droplet deposited on a nylon fiber which is separated from the sample maintained by capillarity between partially overlapping glass plates; b) by an adequate translation the sample is then shifted on the fiber; c) view of the sample from the z direction.

xyz translation stage so that it can be moved as a whole with respect to the nylon (or HPC) fiber the two ends of which are fixed on collinear axes of stepping motors. Thanks to these stepping motors, this second setup allows to control the mechanical torsion of the fiber *in situ* and by this means to change the pitch of the helicoidal anchoring. At the beginning of the experiment the fiber is located outside of the sample and a small droplet of the nematic liquid crystal is deposited on it (see fig. 8a). As mentioned above, for topological reasons the droplet contains a solitary disclination loop threaded on the fiber. Subsequently the nematic sample (NLC + glass plates) is shifted on the fiber in a manner that the disclination is positioned in the sample center. Figure 8c shows a view of such a sample from the z direction. Let us stress that this sample contains in fact two disclination loops: the captive one introduced with the droplet and the pre-existing peripheral disclination loop located in the vicinity of the NLC/air meniscus surrounding the sample [6]. This second disclination loop is free. In thin enough samples this peripheral disclination does not collapse for reasons discussed already in sect. 1.2.

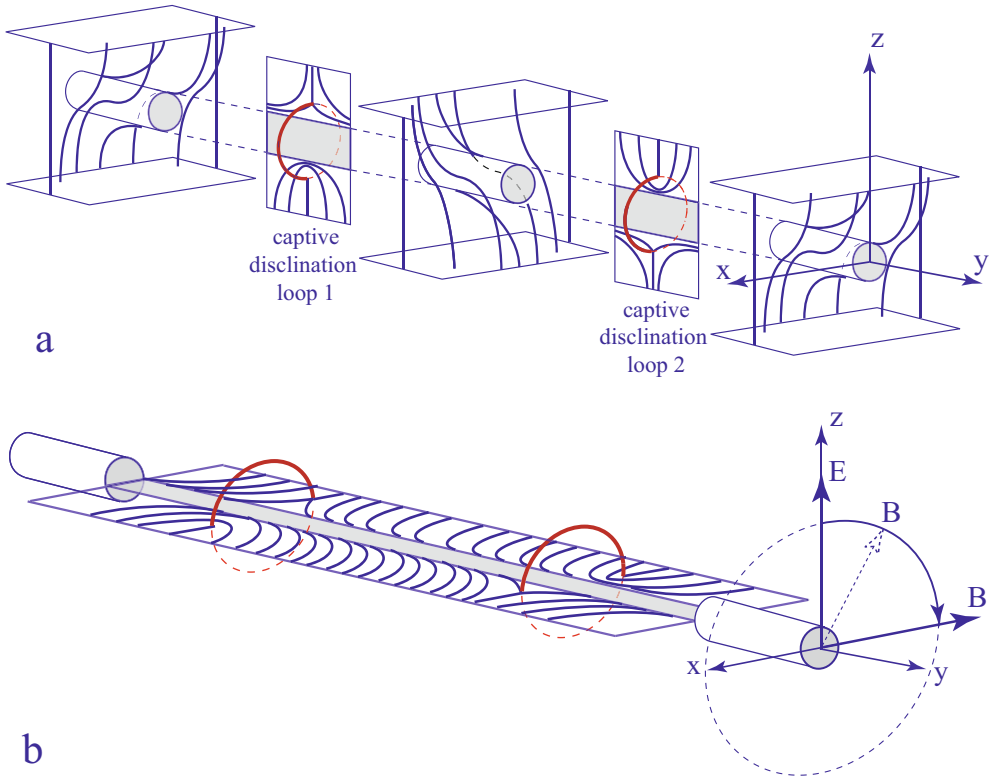

Fig. 9. Distorsion of the director field around two adjacent captive disclinations on a fiber with planar axial anchoring: a) texture in the absence of fields; b) texture rotated by $\pi/2$ due to application of an electric field E in z direction and of a magnetic field B rotated slowly from z to $-x$ direction.

2.3 Captive disclination loops on HPC fibers

The texture of the director field around two adjacent captive disclination loops is shown in fig. 9. It is compatible with the planar axial anchoring on the fiber surface and with the homeotropic anchoring on surfaces of the nematic cell. As we will see further, it explains all features of the chirogyral effect observed in experiments. Before that, it is instructive to show that this texture can be unveiled directly by electrohydrodynamic instabilities in the presence of a magnetic field.

In this experiment, made with the nematic EN18 and with the setup shown in fig. 3, a 1 kHz AC voltage is applied to electrodes. As EN18 has a negative dielectric anisotropy, the electric field **E** favors orientations of the director orthogonal to it. Simultaneously, a magnetic field **B** of 0.05 T is applied to the sample and its direction is slowly rotated around the y axis from the vertical direction ($\mathbf{B}//\mathbf{z}$) to the horizontal one ($\mathbf{B}//-\mathbf{x}$). As a result, the texture shown in fig. 9 rotates as a whole around the y axis and its aspect in a microscope is shown in fig. 10a.

Subsequently a 100 Hz voltage is applied to electrodes. When its amplitude becomes larger than the threshold $V_c = 9$ V of electrohydrodynamic instabilities in the conductive regime [18], convection rolls orthogonal to the local horizontal orientation of the director field appear, as shown in fig. 10b. In this picture, the dashed lines orthogonal to the direction of convection rolls are therefore those of the director field **n**.

Clearly, as expected, this pattern is obtained from the one in fig. 9 by rotation around the y axis in clockwise direction. When the magnetic field is rotated from the z direction by $\pi/2$ in counterclockwise direction, the pattern of convection rolls is changed as shown in fig. 11.

Results of these experiments are important for the forthcoming discussion of the symmetry aspects of the chirogyral effect.

3 Experiments with action of fields on disclination loops

3.1 Tilt of disclination loops on HPC fibers

HPC fibers were drawn by hand from 65-70% HPC/water mixtures in cholesteric phase. In practice, the texture of the sample from which fibers were drawn did not matter because fibers, 10 to 40 μm in diameter, obtained by this method were always optically uniaxial. One could think therefore that HPC macromolecules are aligned and the cholesteric helix is unwound during the elongational flow which results in very high stretching ratios [19]. In such a case, the surface of HPC fibers would produce the axial planar anchoring ($\mathbf{a}//\mathbf{y}$ in fig. 24).

On the basis of symmetry arguments, we expected that disclination loops threaded on our hand-drawn HPC fibers should be orthogonal to their axis **y**. The series of six

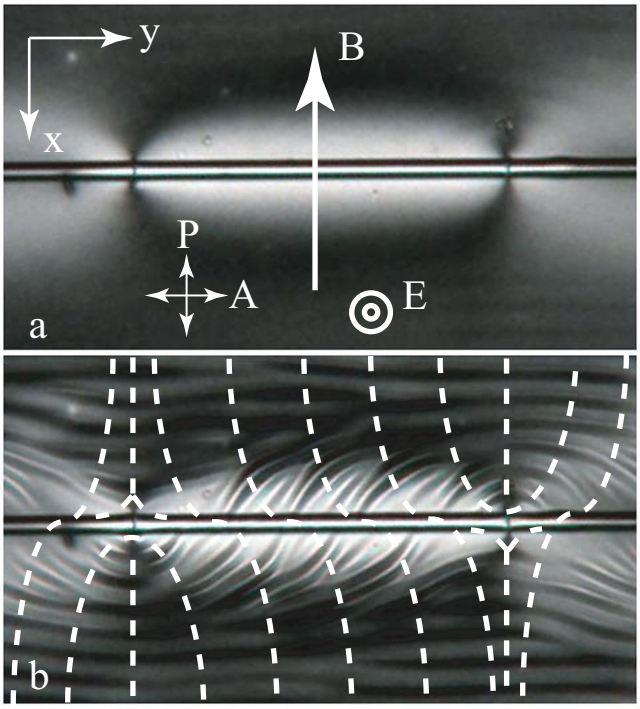

Fig. 10. Distorsion of the director field around two adjacent captive disclinations on a HPC fiber unveiled by electrohydrodynamic instabilities in the presence of a magnetic field B (see fig. 9): a) $V < V_c$; b) $V > V_c$ (nematic EN18 with a negative dielectric anisotropy; $B = 0.05\,\mathrm{T}$).

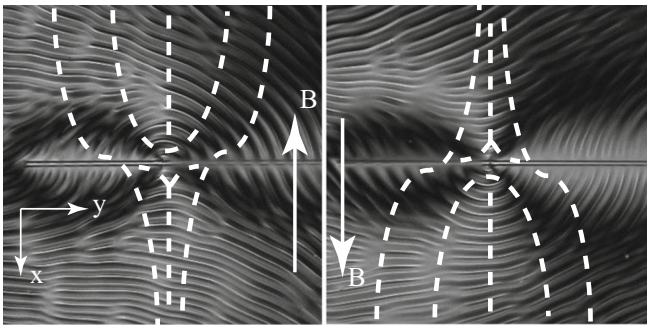

Fig. 11. Electrohydrodynamic instabilities in the presence of a magnetic field B rotated from the z direction by $\pi/2$ in clockwise and anticlockwise directions (nematic EN18 with a negative dielectric anisotropy, $B = 0.05\,\mathrm{T}$).

images shown in fig. 12 proves that this is not the case. At first sight, in the first image labeled "0.00 V" the tilt of the disclination loop is difficult to perceive. However, upon the action of the electric field the tilt of the disclination loop grows considerably. Simultaneously, the loop, seen from the direction **z** of the electric field, changes its shape from a straight one to an S-like. In the image labeled "13.5 V" an oblique line connecting the left and right extremities of the loop makes the angle η with the y axis orthogonal to the fiber. This angle is plotted *versus* the applied AC voltage V_{AC} in fig. 13.

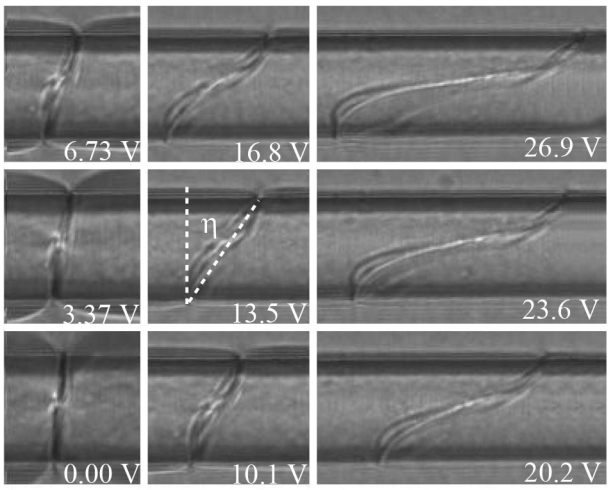

Fig. 12. Views of a disclination loop on a HPC fiber immersed in 5CB and submitted to an electric field generated by an AC voltage (1 kHz) applied to the ITO electrodes. The diameter of the fiber is 40 μm.

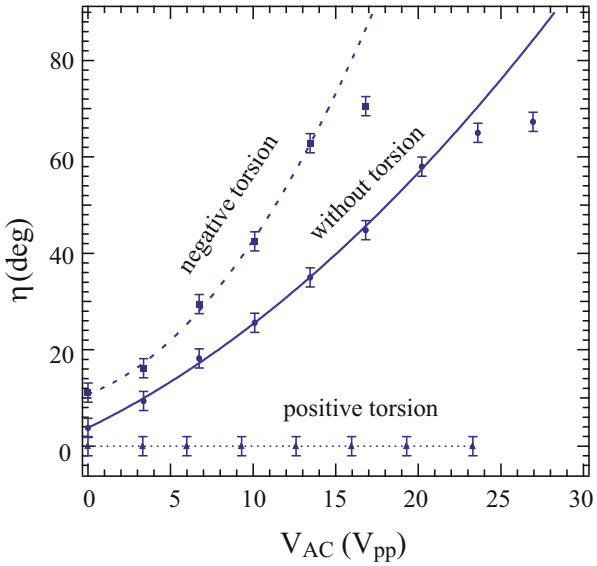

Fig. 13. Plot of the tilt angle η *versus* the AC voltage corresponding to the disclination loop on a HPC fiber shown in fig. 12.

The best polynomial fit of the $\eta(V_{AC})$ dependence given by

$$\eta \approx 3.8\left(1 + 0.44\,V_{AC} + 0.013\,V_{AC}^2 + \ldots\right) \qquad (3)$$

leads to the following conclusions:

1) The disclination loop is tilted in the absence of the field.
2) The tilt angle grows initially linearly with the applied electric field $E = V/d$.

The main conclusion of this first experiment is that, in spite of their uniaxial optical aspect, the HPC filaments drawn by hand produce a helicoidal anchoring on their surface.

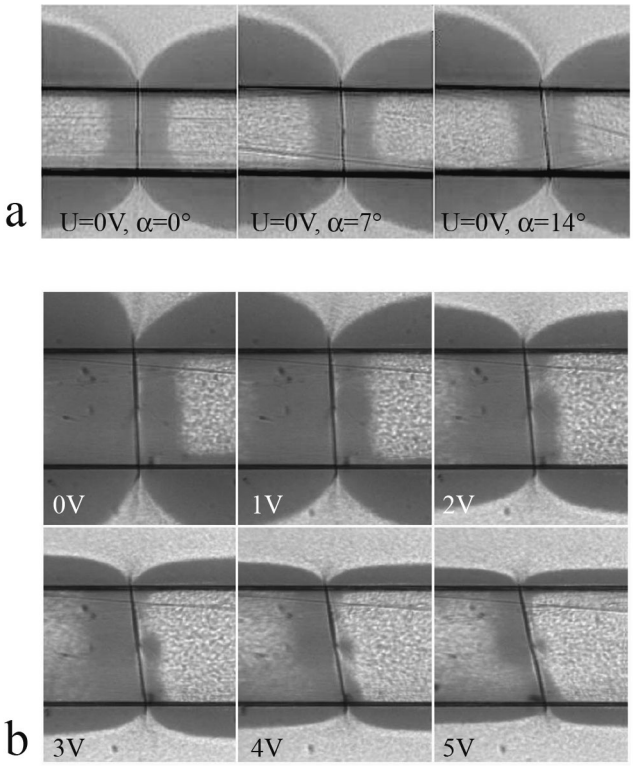

Fig. 14. Chirogyral effect of a disclination loop on a 300 μm nylon fiber immersed in 5CB: a) without electric field, the helix angle is 0, 7 and 14°; b) with an electric field generated by an AC voltage (1 kHz) applied to the ITO electrodes. The diameter of the fiber is 300 μm and its helix angle is $\alpha = 6°$. The fiber is located in the middle of a 5CB sample of thickness $d = 500\,\mu$m.

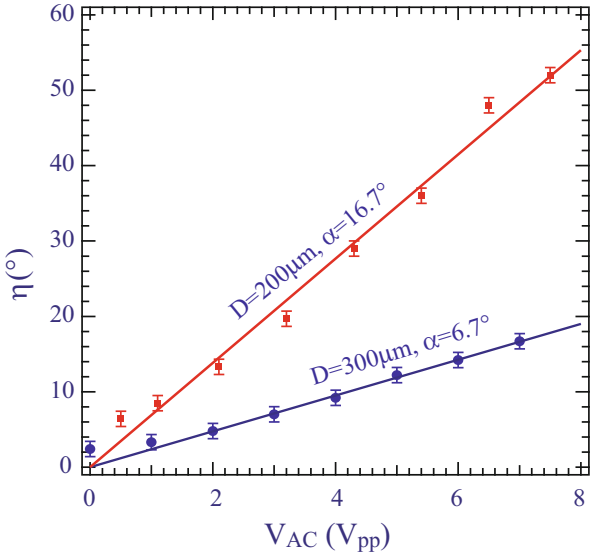

Fig. 15. Plots of the tilt angle η *versus* the AC voltage corresponding to the disclination loops on nylon fibers shown in figs. 14 and 16.

What is the chirality of the helix, left or right? (by the *left chirality* of the helicoidal anchoring we mean the one shown in figs. 4 and 25). With the aim to answer this question, we have submitted the fiber with the disclination loop on it to positive and negative torsions (by the *positive torsion* we mean the one shown in fig. 8). Plots in fig. 13 show that, for a given AC voltage, the negative torsion increases the tilt angle (plot labeled "negative torsion") while the positive torsion decreases it. When it is large enough, it changes the surface anchoring from the helicoidal planar to the planar axial and cancels the chirogyral effect.

Finally we can say that the anchoring on the drawn-by-hand HPC fibers is planar helicoidal and its chirality is left. We will resume this discussion in sect. 5.

3.2 Tilt of captive loops on nylon wires in electric field

With the aim to confirm the sensitivity of disclination loops to the helicity of fibers, another series of experiments was made with a nylon fiber (a fishing wire). Using such fibers with the diameter D of 200 and 300 μm, much larger than the one of HPC fibers, has the advantage to increase precision of measurements of the tilt angle. Another advantage of the nylon fiber is that its torsion, introduced by means of the setup shown in fig. 8, can be changed arbitrarily and measured accurately *in situ*.

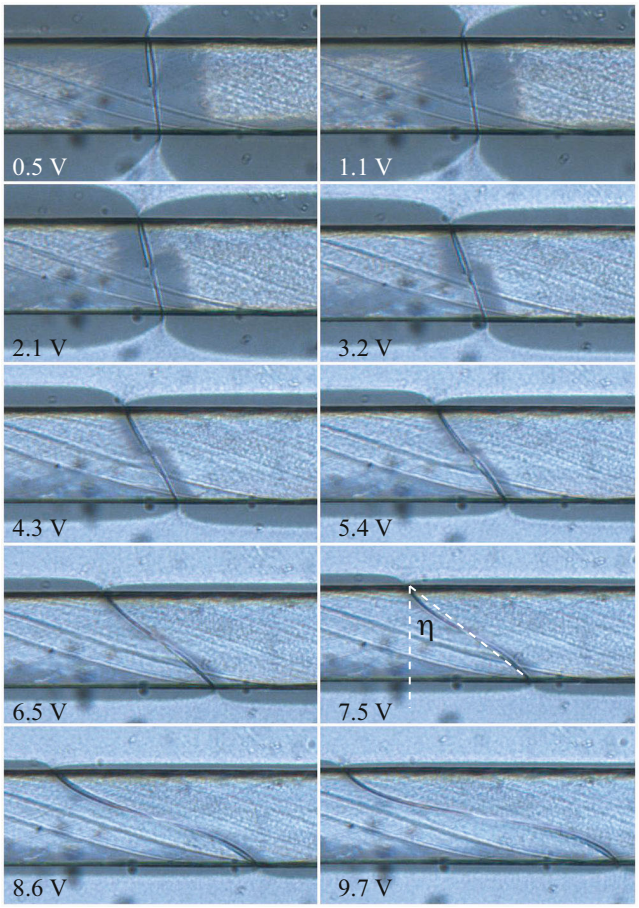

Fig. 16. Views of a disclination loop on a nylon fiber immersed in 5CB and submitted to an electric field generated by an AC voltage (1 kHz) applied to the ITO electrodes. The diameter of the fiber is 200 μm and its helix angle $\alpha = 16.7°$.

First of all, we have seen, as expected, that disclination loops on a non-twisted nylon fiber are perpendicular to it because the polyamide macromolecules are not chiral.

Experiments with twisted nylon fibers submitted to electric fields are illustrated in fig. 14b and 16. In the first experiment (fig. 14b), the torsion angle $\alpha = 6.7°$ is very small so that tilt angles η are small too. In spite of that, thanks to the large diameter $D = 300\,\mu$m of the fiber the optical resolution of the disclination loop is better than in fig. 12 and the tilt angle can be measured with a better accuracy. Results $\eta(V)$ plotted in fig. 15 show a linear dependence on V_{AC} for $V_{AC} > 2V$. We will see in sect. 5 that such a linear dependence $\eta \sim V_{AC}$ is expected for thick fibers.

In the second experiment made with a nylon fiber of diameter $D = 200\,\mu$m, the angle of the torsion $\alpha = 16.7°$ is larger so that the tilt angles are larger too. Moreover, for $V_{AC} > 5V$ the disclination loop takes an S-like shape. In such a case a straight line is drawn between extremities of the loop and the angle η is measured as shown in the image labeled "7.5 V". Once again, the results $\eta(V_{AC})$ plotted in fig. 15 show a linear dependence on V_{AC} for $V_{AC} > 2V$.

3.3 Tilt of captive loops on nylon wires in magnetic field

Experiments on the chirogyral effect with disclination loops on twisted nylon fibers submitted to a magnetic field are illustrated in figs. 17, 18, and 19 in which the magnetic

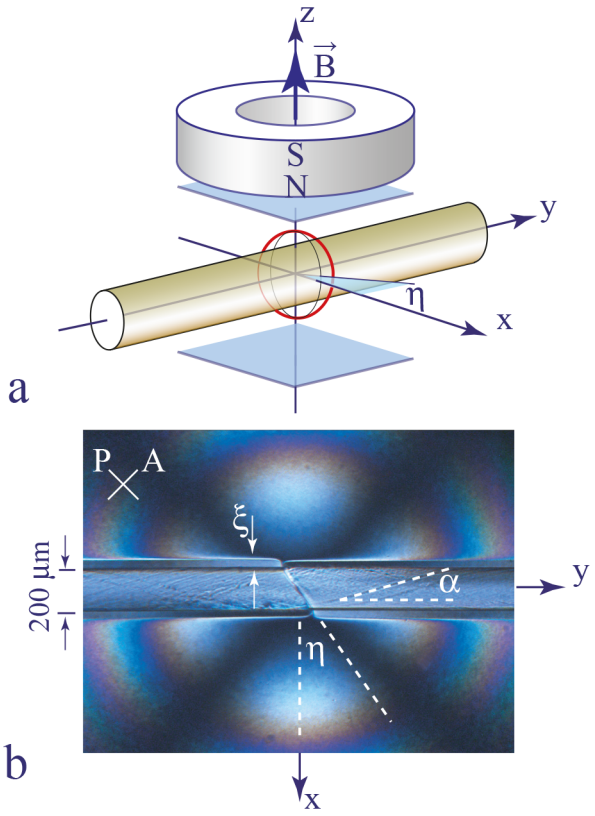

Fig. 17. Chirogyral effect in a vertical magnetic field: a) perspective view of the setup; b) view of the sample from z direction.

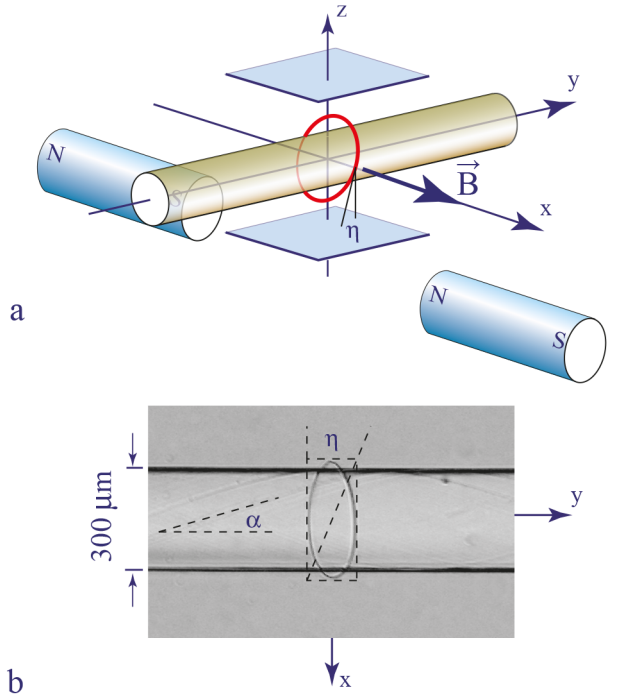

Fig. 18. Chirogyral effect in a horizontal magnetic field: a) perspective view of the setup; b) view of the sample from z direction.

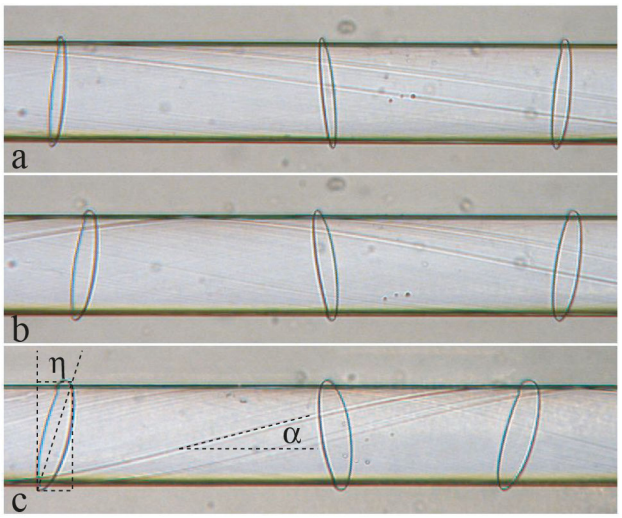

Fig. 19. Views of three adjacent disclination loops on a twisted nylon fiber immersed in 5CB and submitted to an oblique magnetic field. The diameter of the fiber is 200 μm. The torsion of the fiber increases from a to c. Stripes visible on the fiber surface allow to measure directly the helix angle α defined in fig. 4.

field is respectively vertical (parallel to the z axis) horizontal (parallel to the x axis) and oblique (parallel to the zx plane and making the angle of $\theta_B \approx 60°$ with the z axis).

The aspect of the disclination loop tilted by the vertical magnetic field in fig. 17b is the same as in the case of the electric field discussed above. The horizontal field

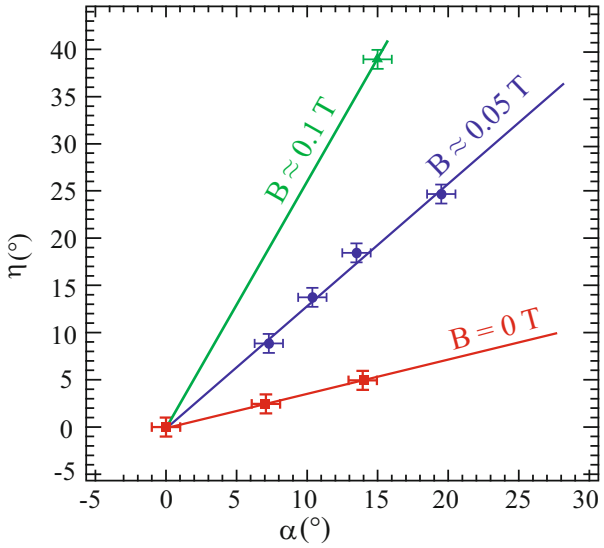

Fig. 20. Plot of the tilt angle η *versus* the helix angle corresponding to the disclination loops on twisted nylon fibers shown in figs. 17 (triangular marker), fig. 18 (circular markers) and fig. 14a (square markers).

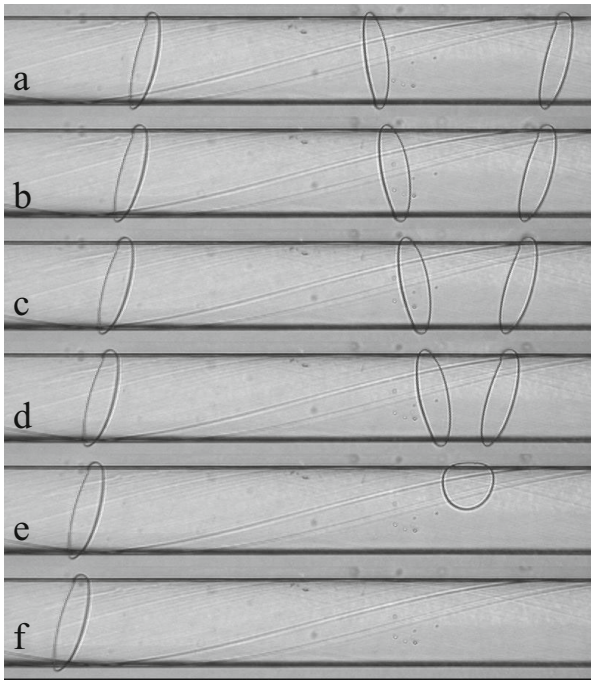

Fig. 21. Translation of disclination loops on the nylon fiber induced by a magnetic field oblique with respect to the fiber axis z. The angle θ_B defined in fig. 3 is $\approx 30°$. Images a to f have been taken at intervals of 100 s. The two loops on the right meet and coalesce into one loop which collapses.

makes the disclination loop rotate around the x axis so that its aspect in fig. 18b is elliptical. Finally, the action of an oblique field is illustrated by the series of three photographs in fig. 19. We see here three adjacent disclination loops which appear as oblique ellipses. In this case, the tilt angle η of the chirogyral effect is determined from a simple geometrical construction defined in fig. 19c.

From these all three aspects (line, ellipse, oblique ellipse) of disclination loops we can infer that the disclination loops rotate around the direction of the magnetic field. In the theoretical section we will see that this should be the case when the magnetic coherence length ξ is much shorter than the sample thickness d. Actually, in fig. 17b the coherence length $\xi \approx 35\,\mu$m is 5.6 times smaller than the fiber diameter of 200 μm which is inserted in a sample of thickness $d \approx 500\,\mu$m.

In the experiment of fig. 19, the magnetic field **B** is tilted in the xz plane and makes with the **z** axis the angle $\phi_B = -60°(\theta_B = 0)$. Its intensity B is also kept constant but the torsion of the nylon fiber is varied. The corresponding helix angle α can be measured on images in fig. 19. Clearly, for $B \approx 0.05\,$T, the tilt angle η grows with the torsion of the fiber.

Results of this experiment, plotted with circular markers in fig. 20, correspond well to a linear fit

$$\eta = C\alpha, \tag{4}$$

with $C(0.05\,\mathrm{T}) = 1.3$. In the same fig. 20, square markers represent measurements of η and α made without fields (see the three pictures in fig. 14a). The corresponding chirogyral coefficient is $C(0\,\mathrm{T}) = 0.34$. Finally, in the experiment with the vertical field (see fig. 17) of intensity $B \approx 0.1\,$T the chirogyral coefficient is $C(0.1\,\mathrm{T}) = 2.6$.

3.4 Translation of disclination loops induced by an oblique field

When the magnetic field **B** is oblique with respect to the fiber axis **y**, it drives a translation of disclination loops. This is illustrated by the series of six pictures shown in fig. 21. The velocity of motion is about 0.4 μm/s. Adjacent loops move in opposite directions. As a result, the two loops on the right converge, meet and coalesce into one loop. Being located outside the fiber this loop coalesces.

3.5 Behavior of charged captive disclination loops

Let us discuss now the chirogyral effect in the case of a charged captive disclination loop which can be obtained, for example, by fusion of a neutral disclination loop with a monopole as shown in fig. 22.

These two defects (that exist on their own in fig. 22a) stem from the texture shown previously in fig. 8c: the captive disclination loop persists while the monopole is created by the collapse of the peripheral disclination when the aspect ratio between the sample thickness d and the radius of the peripheral disclination R is increased about a critical value given by eq. (1). Upon a subsequent decrease of the sample thickness to its initial value, the monopole and the dowser texture around it persist in spite of their metastability. The series of four pictures a–c in fig. 22 shows that the monopole, which can be considered as a minimal charged disclination loop, is attracted toward the neutral disclination loop and by their coalescence a charged captive disclination loop is obtained (see fig. 22d).

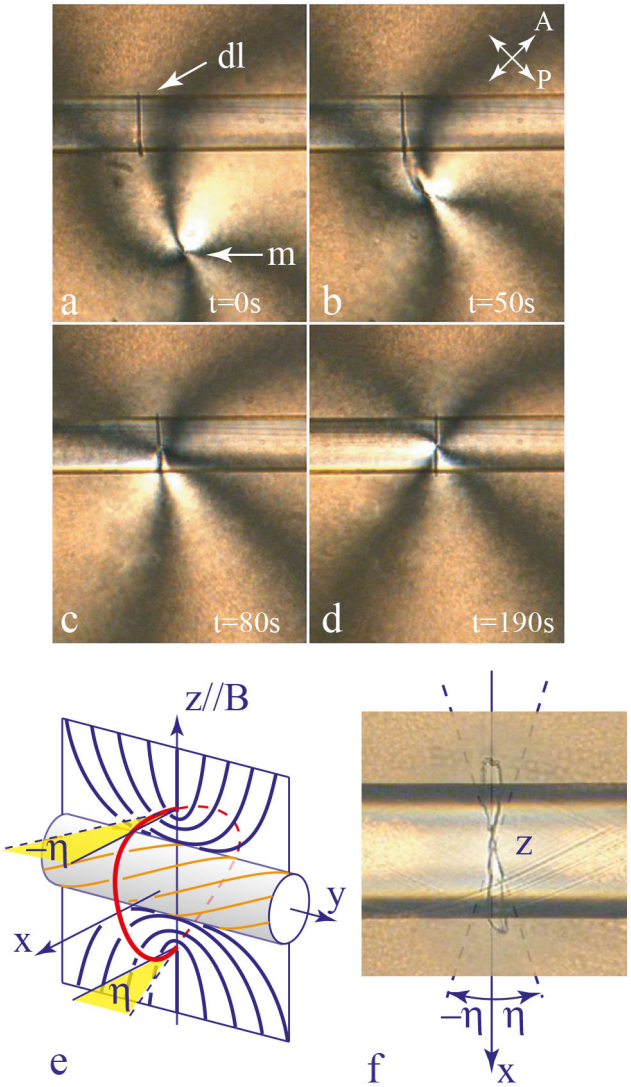

Fig. 22. Chirogyral effect of a charged disclination loop: a–d) generation of a charged disclination loop by fusion of a neutral disclination loop (dl) with a monopole (m); e) texture around the charged disclination loop; f) deformation of the charged loop due to the chirogyral effect. (200 μm nylon fiber immersed in MBBA).

The texture surrounding this captive charged disclination loop is depicted in fig. 22e. It is symmetrical with respect to the mirror symmetry in the xy plane. For this reason, the sign of the chirogyral effect is opposite in the upper ($z > 0$) and lower ($z < 0$) halves of the disclination loop so that, when observed along the z axis (parallel to the magnetic field), the disclination loop threaded on a twisted nylon fiber has a characteristic figure-eight shape.

4 Analytical model

4.1 Axial planar anchoring

Let us consider first a cylinder with planar axial anchoring **a**//**y**, immersed in a nematic. In the absence of fields and other surface conditions the director field **n** would take the direction parallel to the cylinder axis **y**. The symmetry of this ground state is $D_{\infty h}$ (see fig. 23a).

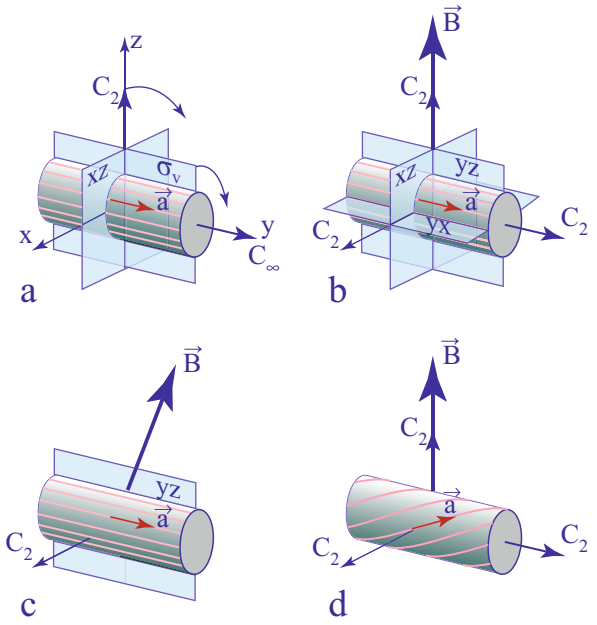

Fig. 23. Symmetries of the system "cylinder + field". a) Planar axial anchoring, no field: $D_{\infty h}$, for simplicity only one mirror plane parallel to the cylinder axis and one twofold axis orthogonal to it are shown; b) planar axial anchoring + field orthogonal to the cylinder: D_{2h}; c) planar axial anchoring + field oblique to the cylinder: C_{2v}; d) helical anchoring + field orthogonal to the cylinder: D_2.

When a magnetic field **B** is applied in the direction **z** orthogonal to the cylinder, the symmetry $D_{\infty h}$ is broken into D_{2h} (see fig. 23b) and the director field will be distorted: far from the cylinder it will take the direction of the field while on the cylinder surface it will remain parallel to **y**.

As shown in fig. 24 two distorted ground states **a** and **b** are possible. Taken separately they are symmetrical only with respect to the longitudinal mirror plane yz and to the twofold axis C_2//**x** orthogonal the field. All other symmetry operations of the group D_{2h} (mirror planes xy and xz and the two-fold axis C_2//**B**) exchange the two ground states.

The same symmetry breaking occurs when the cylinder immersed in a nematic is submitted to the action of glass plates with homeotropic anchoring [15].

In the two ground states generated by the magnetic field, the distorsion is localized in a cylindrical shell the thickness of which is given by the so-called magnetic coherence length ξ (see sect. 3.2.2 in ref. [18]). In the approximation of isotropic elasticity ($K_1 = K_2 = K_3 = K$)

$$\xi(B) = \sqrt{\frac{\mu_o K}{\chi_a}} \frac{1}{B} \tag{5}$$

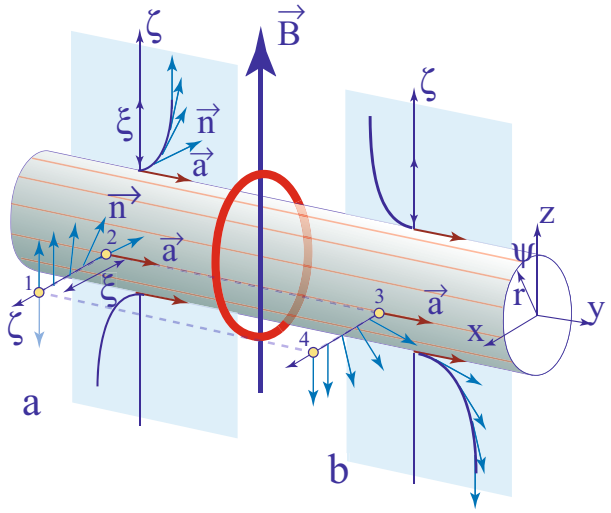

Fig. 24. Fiber with axial anchoring in the magnetic field orthogonal to it: a and b are the two ground states.

and the elastic energy per unit surface of the distorted boundary layer is given by

$$F = \frac{1}{2}\frac{K}{\xi}\,. \tag{6}$$

4.2 Tilted magnetic field, translation of disclination loops

When the magnetic field is oblique to the cylinder (for example tilted in the direction of the **y** axis, as shown in fig. 23c), the symmetry D_{2h} is broken to C_{2v} and the two ground states are no more related by any symmetry operation. If the angle between the magnetic field and cylinder is written as

$$\frac{\pi}{2} - \theta_B = \frac{\pi}{2}(1-\epsilon), \tag{7}$$

where $\epsilon \ll 1$, then the distortion energy of states **a** and **b** becomes

$$F_{a/b} = (1 \mp \epsilon)^2 \frac{K}{2\xi}\,. \tag{8}$$

When the two possible states **a** and **b** coexist on the fiber, there must be a disclination loop at the junction between them. This can be easily checked by following the director orientation on the circuit 12341 drawn with dashed line in fig. 24. At the starting point 1 the director is $(0, 0, 1)$ while after the whole turn of the circuit it becomes $(0, 0, -1)$.

The energies per unit surface of the boundary layers adjacent to the disclination loop F_a and F_b can be seen as forces per unit length pulling on the loop, respectively, in $-\mathbf{y}$ and $\mathbf{y}$ directions. The resultant force

$$f = F_a - F_b = \frac{2K}{\xi}\epsilon \tag{9}$$

will pull the loop in the **y** direction when the tilt angle of the magnetic field $\theta_B = \epsilon\frac{\pi}{2}$ is positive. As a result, the disclination loop will move in the **y** direction, as observed in experiments.

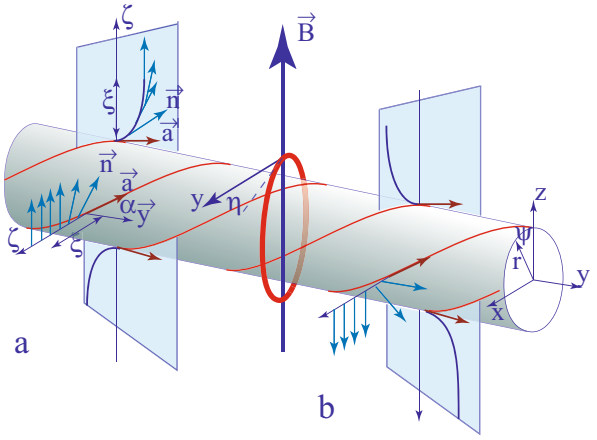

Fig. 25. Fiber with helicoidal anchoring in the magnetic field orthogonal to it: a) and b) are the two ground states related by the twofold symmetry axis C_2 parallel to the x axis.

When other disclination loops coexist on the fiber then their sequence can represented as

$$\mathbf{a} - DL_1 - \mathbf{b} - DL_2 - \mathbf{a} - DL_3 - \mathbf{b} \ldots . \tag{10}$$

In this sequence, the ground states **a** and **b** are located respectively on left and right sides of loops DL_1 and DL_3 as it is shown in fig. 24. In the case of the loop DL_2 the positions of the ground states are inverted so that the force f given by eq. (9) changes its sign. This explains the behavior of the three loops in fig. 21.

4.3 Helicoidal planar anchoring

In the case of the helicoidal anchoring the anchoring direction **a** can be written as

$$\mathbf{a} = [\sin(\alpha)\sin(\psi), \sin(\alpha)\cos(\psi), \cos(\alpha)], \tag{11}$$

where α is the angle between **a** and the helix axis **y** while ψ is the angle of the cylindrical coordinates (r, ψ, y). When the magnetic field **B** is, for example, parallel to **z** then the angle β between **B** and **a** is given by

$$\beta = \arccos[\sin(\alpha)\sin(\psi)]. \tag{12}$$

In the boundary layer of type **a** shown in fig. 25a the angle γ between the director and the magnetic field decreases from β to zero on the distance ξ

$$\gamma(\zeta) = \beta\frac{2\arctan[\exp(-\zeta/\xi)]}{\pi/2}\,, \tag{13}$$

while in the boundary layer of the second type **b** the angle γ grows from β to π:

$$\gamma(\zeta) = \pi - (\pi-\beta)\frac{2\arctan[\exp(-\zeta/\xi)]}{\pi/2}\,. \tag{14}$$

The elastic energy per unit area of the boundary layer is then given by

$$F_a = \frac{1}{2}K\int_0^\infty \left(\frac{\mathrm{d}\gamma}{\mathrm{d}\zeta}\right)^2 \mathrm{d}\zeta = \frac{K}{2\xi}\left(\frac{\beta}{\pi/2}\right)^2 \tag{15}$$

for the type **a** and by

$$F_b = \frac{K}{2\xi}\left(\frac{\pi-\beta}{\pi/2}\right)^2 \tag{16}$$

for the type **b**.

When α is small, one has

$$\beta = \frac{\pi}{2} - \sin(\alpha)\sin(\psi) \tag{17}$$

and one gets approximatively

$$F_{a/b} \approx \frac{K}{2\xi}\left(1 \pm \frac{4\sin(\alpha)\sin(\psi)}{\pi}\right). \tag{18}$$

4.4 Field-induced tilt of disclination loops

We know already that when the two ground states **a** and **b** occur alternatively on the fiber, disclination loops must occur at junctions between them. Due to the dependence of $F_{a/b}$ on the cylindrical coordinate ψ, there is a force per unit length acting on the disclination loop

$$f = F_a - F_b \approx \frac{K}{\xi}\frac{4\sin(\alpha)}{\pi}\sin(\psi) \tag{19}$$

This force has to be balanced by a deformation of the loop. Let $\delta(\psi)$ be the displacement of the loop in the **y** direction. In coordinates $(\delta, R\psi)$ the disclination loop looks like a string with tension T (see fig. 26b). In equilibrium, the restoring force due to the curvature of the tense string will balance the force f

$$-T\frac{\frac{1}{R^2}\frac{\mathrm{d}^2\delta}{\mathrm{d}\psi^2}}{\sqrt{1+\frac{1}{R^2}(\frac{\mathrm{d}\delta}{\mathrm{d}\psi})^2}} = \frac{K}{\xi}\frac{4\sin(\alpha)}{\pi}\sin(\psi). \tag{20}$$

For small deformations one obtains

$$-\frac{\mathrm{d}^2\delta}{\mathrm{d}\psi^2} = \delta_o\sin(\psi) \tag{21}$$

with

$$\delta_o = \frac{4}{\pi}\frac{K}{T}\frac{R^2}{\xi}\sin(\alpha), \tag{22}$$

so that

$$\delta = \delta_o\sin(\psi). \tag{23}$$

If one looks at the loop from the direction of the magnetic field then

$$\eta = \frac{\delta_o}{R} = \frac{4}{\pi}\frac{K}{T}\frac{R}{\xi}\sin(\alpha) \tag{24}$$

is the angle that the loop makes with the xz plane.

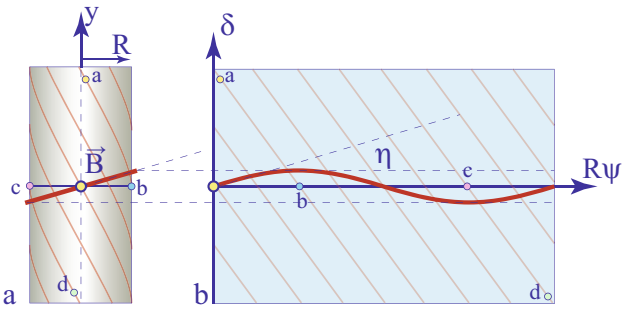

Fig. 26. Tilt of the disclination loop induced by the magnetic field: a) view of the fiber from the direction of the magnetic field; b) flattened representation of the fiber surface.

5 Discussion and conclusions

5.1 Chirogyral effect in fields: detection of helicity

In the limit $\xi \ll D$, the chirogyral coefficient in eq. (24) is thus inversely proportional to the magnetic coherence length $\xi(B)$ defined in eq. (5). This result can be easily transposed to the case of the electric field **E** acting on nematics with the positive dielectric anisotropy ϵ_a writing

$$\xi(E) = \sqrt{\frac{K}{\epsilon_o\epsilon_a}}\frac{1}{E}. \tag{25}$$

In the limit $\xi(E) \ll D$, the chirogyral coefficient is thus proportional to the intensity of the electric field $|\mathbf{E}|$. From the previous work [15] we know that in the limit $\xi \to \infty$, that is to say $E \to 0$, the value C_{go} of the chirogyral coefficient depends on the ratio between the diameter $D = 2R$ of the fiber and the thickness d of the cell. In summary, the dependence of the chirogyral coefficient on the field intensity can be written as:

$$C_g = C_{go}(1 + AE + BE^2 + \ldots). \tag{26}$$

These theoretical results explain the experimentally observed variation of the tilt angle with the intensity of the electric field plotted in fig. 13. In conclusion, when the nematic has a positive dielectric anisotropy, *the application of the electric field enhances the chirogyral effect and allows to detect a very small helicity of fibers.*

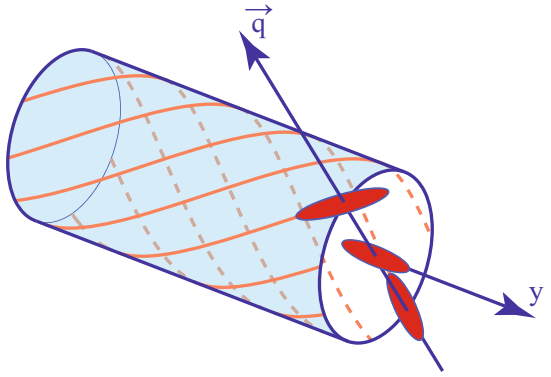

Fig. 27. Relationship between the helicity of the anchoring and the handedness of the cholesteric texture.

The second result of this experiment is that the chirogyral effect can be canceled by submitting the HPC fiber to an adequate positive torsion. This means that the anchoring on the surface of the HPC fiber drawn by hand is helicoidal and left-handed as shown in fig. 27. During the drawing of the fiber from the anisotropic HPC/water solution the polymer solution is submitted to an elongational flow resulting in a large stretching ratio. The birefringence of fibers drawn by this method is close to the saturation. One can think therefore that the bulk of the HPC fibers has the double twist right-handed texture shown in fig. 27. This right-handedness of the cholesteric helix of HPC agrees with conclusions of the optical measurements made by Werbowyj and Gray [20]. *Our method allows thus to measure the helicity of fibers.*

5.2 Translation and merging of disclination loops

We have also pointed out that captive disclination loops can be set in motion by magnetic fields oblique to fibers. The direction of this translation is opposite for adjacent disclinations. By an adequate choice of the direction of the magnetic field, these motions can be made converging so that merging of adjacent disclination loops becomes possible. This effect is suitable for *conception of micromechanical and microfluidic systems* in which the captive disclination loops would transport substances contained in their cores.

We thank H. Kitzerow, P. Keller and I. Dozov who offered us nematic materials EN18, MBBA and 5CB used in this study. The authors also thank V. Klein, S. Saranga, J. Sanchez, J.-L. Signoret, M. Bottineau, J. Vieira et A. Lecchi for technical help. M.H.G. acknowledge funding from FEDER through the COMPETE 2020 Program and National Funds through FCT-Portuguese Foundation for Science and Technology under projects UID/CTM/50025/2013. S. Č. acknowledges support by Slovenian Research Agency (ARRS) under grants P1-0099 and Z1-6725.

Author contribution statement

All authors contributed equally to the paper.

References

1. G. Friedel, Ann. Phys. **18**, 273 (1922).
2. V.S.U. Fazio, L. Komitov, S.T. Lagerwall, Liq. Cryst. **24**, 427 (1998).
3. V.S.U. Fazio, L. Komitov, Europhys. Lett. **46**, 38 (1999).
4. V.S.U. Fazio, L. Komitov, C. Raduge, S.T. Lagerwall, H. Motschmann, Eur. Phys. J. E **5**, 309 (2001).
5. P. Oswald, P. Pieranski, *Nematic and Cholesteric Liquid Crystals* (Taylor&Francis, 2005) see Fig. B.IV.18.
6. P. Pieranski, M.H. Godinho, S. Čopar, Phys. Rev. E **94**, 042706 (2016).
7. R.W. Ruhwandl, E.M. Terentjev, Phys. Rev. E **56**, 5561 (1997).
8. H. Stark, Eur. Phys. J. B **10**, 311 (1999).
9. J.C. Loudet, P. Poulin, Phys. Rev. Lett. **87**, 165503-1 (2001).
10. I. Musevič, M. Škarabot, U. Tkalec, M. Ravnik, S. Žumer, Science **313**, 954 (2006).
11. Y. Geng, P.L. Almeida, J.L. Figueirinhas, E.M. Terentjev, M.H. Godinho, Soft Matter **8**, 3634 (2012).
12. Y. Geng, D. Seč, P.L. Almeida, O.D. Lavrentovich, S. Žumer, M.H. Godinho, Soft Matter **9**, 7928 (2013).
13. M. Nikkhou, M. Škarabot, S. Čopar, M. Ravnik, S. Žumer, I. Muševič, Nat. Phys. **11**, 183 (2015).
14. M. Nikkhou, M. Škarabot, I. Muševič, Eur. Phys. J. E **38**, 23 (2015).
15. S. Čopar, D. Seč, L.A. Aguire, P.L. Almeida, M. Dazza, M. Ravnik, M.H. Godinho, P. Pieranski, S. Žumer, Phys. Rev. E **93**, 032703 (2016).
16. L.E. Aguirre, A. de Olivera, D. Seč, S. Čopar, P.L. Almeida, M. Ravnik, M.H. Godinho, S. Žumer, Proc. Natl. Acad. Sci. U.S.A. **113**, 1174 (2016).
17. K.A. Takeuchi, M. Sano, Phys. Rev. Lett. **104**, 230601-1-4 (2010).
18. P.-G. de Gennes, J. Prost, *The Physics of Liquid Crystals*, 2nd edn. (Oxford University Press, 1993) chapt. 5.3.
19. M.H. Godinho, P. Pieranski, P. Sotta, Eur. Phys. J. E **39**, 89 (2016).
20. R.S. Werbowyj, D.G. Gray, Macromolecules **17**, 1512 (1984).